

See discussions, stats, and author profiles for this publication at: <https://www.researchgate.net/publication/303501440>

Coupling the WRF model with a temperature index model based on remote sensing for snowmelt simulations in a river basin in the Altay Mountains, northwest China: Snowmelt simulation...

Article in *Hydrological Processes* · May 2016

DOI: 10.1002/hyp.10924

CITATIONS

8

READS

208

7 authors, including:



Xuejiao Wu

Chinese Academy of Sciences

11 PUBLICATIONS 58 CITATIONS

[SEE PROFILE](#)



Yongping Shen

Cold and Arid Regions Environmental and Engineering Research Institute, Chinese Academy of Sciences

76 PUBLICATIONS 2,497 CITATIONS

[SEE PROFILE](#)



Ninglian Wang

Chinese Academy of Sciences

148 PUBLICATIONS 2,540 CITATIONS

[SEE PROFILE](#)



Xiaoduo Pan

Chinese Academy of Sciences

28 PUBLICATIONS 285 CITATIONS

[SEE PROFILE](#)

Some of the authors of this publication are also working on these related projects:



MELTING EARTH: Glacier Retreat and its Impacts in China's Cryosphere [View project](#)



Microbial ecology [View project](#)

Coupling the WRF model with a temperature index model based on remote sensing for snowmelt simulations in a river basin in the Altay Mountains, north-west China

Xuejiao Wu,^{1*} Yongping Shen,² Ninglian Wang,^{1,3} Xiaoduo Pan,¹ Wei Zhang,¹ Jianqiao He¹ and Guoya Wang⁴

¹ State Key Laboratory of Cryosphere Sciences, Cold and Arid Regions Environmental and Engineering Research Institute, Chinese Academy of Sciences, Lanzhou 730000, China

² State Key Laboratory of Frozen Soil Engineering, Cold and Arid Regions Environmental and Engineering Research Institute, Chinese Academy of Sciences, Lanzhou 730000, China

³ CAS Center for Excellence in Tibetan Plateau Earth Sciences, No. 16 Lincui Road, Chaoyang District, Beijing 100101, China

⁴ Geological Hazards Prevention Institute, Gansu Academy of Sciences, Lanzhou 730000, China

Abstract:

Snowmelt water is an important freshwater resource in the Altay Mountains in north-west China; however, warming climate and rapid spring snowmelt can cause floods that endanger both public and personal property and safety. This study simulates snowmelt in the Kayiertesi River catchment using a temperature index model based on remote sensing coupled with high-resolution meteorological data obtained from National Centers for Environmental Prediction (NCEP) reanalysis fields that were downscaled using the Weather Research Forecasting model and then bias corrected using a statistical downscaled model. Validation of the forcing data revealed that the high-resolution meteorological fields derived from the downscaled NCEP reanalysis were reliable for driving the snowmelt model. Parameters of the temperature index model based on remote sensing were calibrated for spring 2014, and model performance was validated using Moderate Resolution Imaging Spectroradiometer snow cover and snow observations from spring 2012. The results show that the temperature index model based on remote sensing performed well, with a simulation mean relative error of 6.7% and a Nash–Sutcliffe efficiency of 0.98 in spring 2012 in the river of Altay Mountains. Based on the reliable distributed snow water equivalent simulation, daily snowmelt run-off was calculated for spring 2012 in the basin. In the study catchment, spring snowmelt run-off accounts for 72% of spring run-off and 21% of annual run-off. Snowmelt is the main source of run-off for the catchment and should be managed and utilized effectively. The results provide a basis for snowmelt run-off predictions, so as to prevent snowmelt-induced floods, and also provide a generalizable approach that can be applied to other remote locations where high-density, long-term observational data are lacking. Copyright © 2016 John Wiley & Sons, Ltd.

KEY WORDS high mountain hydrology; snow water equivalent distribution; Weather Research Forecasting model; positive air temperature; snowmelt water volume

Received 6 December 2015; Accepted 15 May 2016

INTRODUCTION

Global warming and other human-induced environmental changes are having increasingly severe impacts on the cryosphere (IPCC, 2013). Snow cover is an important component of the cryosphere, and alpine snow distribution and its subsequent melt can dominate local and regional hydrology in mountainous regions. In the short term, faster snowmelt will lead to an increased risk of local flooding, avalanches and other snow disasters in

mountainous areas during spring. These events threaten public and private property and the safety of citizens. In north-west China, snowmelt floods occur mainly in the Altay and Tacheng areas, and along the northern slopes of the Tianshan Mountains in north Xinjiang (Shen *et al.*, 2013). An understanding of how snow water resources are distributed throughout high mountain basins is therefore critical for water resource planning in these regions. Ground-based observations of catchment-scale snow water equivalent (SWE) are challenging because of difficult access and avalanche danger (Dozier and Painter, 2004). Available point-based observations have limited use in snowmelt predictions and are outpaced by remote sensing and modelling (Rice and Bales, 2010). Coupling climate and snowmelt models has great potential for

*Correspondence to: Xuejiao Wu, State Key Laboratory of Cryosphere Sciences, Cold and Arid Regions Environmental and Engineering Research Institute, Chinese Academy of Sciences, Lanzhou 730000, China.
E-mail: xjwu@lzb.ac.cn

calculating the distribution of SWE at high spatial resolution and for making reliable snowmelt predictions.

Snowmelt simulation can help understand and effectively make use of snowmelt water resource. Current snowmelt models can generally be classified into two categories: empirical temperature index models (TIMs) (Reeh, 1989; Hock, 1999), such as the degree-day model, and physically based energy balance models (Ma *et al.*, 1991). Energy balance models use physically based calculations of heat exchanges without a strong regional dependence. However, they require accurate data and include complex parameterization processes. TIMs require fewer static parameters and less complex data compared with energy balance models (Ohmura, 2001). Also, because air temperature is generally the most readily available data, TIMs have been widely used for modelling ice melt/snowmelt and ice dynamics, and for climate sensitivity studies (Hock, 2003) in areas such as Greenland, northern Europe and the Qinghai–Tibet Plateau (Gao *et al.*, 2012; Box, 2013; Matthews *et al.*, 2015). As such, TIMs are also frequently applied in sparsely monitored basins, have been shown to provide reliable snowmelt estimates (Jost *et al.*, 2012), and are suitable for use in catchment-scale research (Irvine-Fynn *et al.*, 2014).

Spatial meteorological forcing data play a major role in snowmelt models and other distributed hydrological and ecological models (Pan *et al.*, 2012). Meteorological data gathered by national organizations are commonly used as forcing data for snowmelt run-off or hydrological models. Another approach is to interpolate meteorological data from an array of weather stations to force a distributed model. However, weather station data are restricted by the locations of weather stations. A new method has been proposed, involving coupling or using climate model outputs as forcing data for hydrological and ecological models (Zhao *et al.*, 2009). The Weather Research Forecasting (WRF) model has been modified for application over longer timescales than the typical, numerical weather model. As boundary conditions, it can use either reanalysis fields, to simulate the observed past, or global climate model output fields, to simulate the future. Here, we use WRF in retrospective mode with National Centers for Environmental Prediction (NCEP) boundary conditions to produce high-resolution 5-km gridded meteorological fields over the study area for spring 2012. WRF output fields are then bias corrected and spatially disaggregated to 1 km using a statistical model, before being used as input to the TIM to simulate snowmelt processes in a river basin in the Altay Mountains in north-west China.

In the snowmelt model, remote sensing data also play a key role in parameterization to minimize the number of parameterizations and make the model easily applicable

to data-poor regions. The aim of this study is to test the ability of the NCEP-based downscaled high-resolution meteorology data for use as meteorological forcing data in mountainous areas, and to assess the simulation capacity of the improved temperature index snowmelt model based on remote sensing data. It is hoped that the results will improve our understanding of spring SWE distribution and snowmelt process in mountainous regions and provide a basis for the prevention of snowmelt-induced flooding in spring. It is also hoped that TIM based on remote sensing data could be considered for wide use in data-poor regions.

METHODS

This section begins with a description of the study area and available stations with meteorological and hydrological measurements. This is followed by an outline of the snowmelt model and the production of meteorological forcing data. The parameters incorporated into the snowmelt model are introduced, then model evaluation methods are described.

Study site and station descriptions

The study area is located in the Kayiertesi River basin in the Altay Mountains in northern Xinjiang. The basin is the headwaters of the Eerqisi River (Figure 1). The climate of this region is influenced by westerly airflow, and most annual precipitation falls as snow, which creates a thick and stable winter snow cover. The drainage area of the basin, calculated using digital elevation model data at high spatial resolution (30 × 30 m), is 2350 km², and the altitude ranges from 1159 to 3846 m above sea level (a.s.l.).

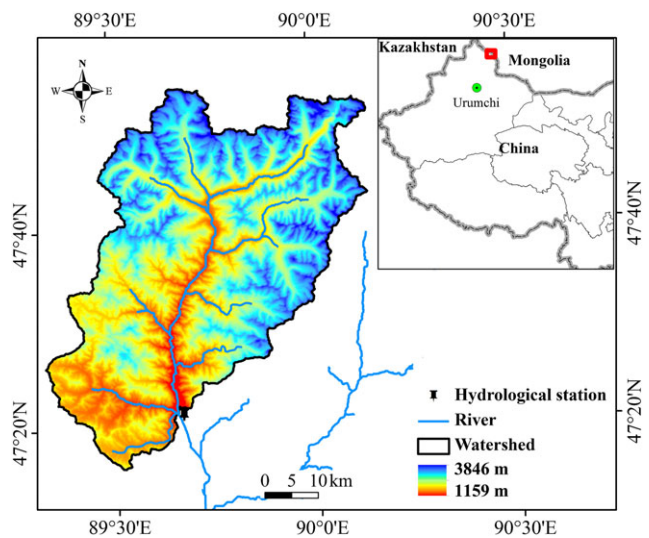


Figure 1. Map showing the geographic characters and location of the study basin

The area has a cool climate with a mean annual temperature of 3.0°C for the period 1962–2012. Snowmelt begins in March (monthly mean temperature of –6.3°C). Mean annual precipitation is 190.7 mm for 1962–2012, and the two months with the lowest mean precipitation are February (8.1 mm) and March (10.5 mm).

Our observation site is located at Kuwei Hydrologic Station at the outlet of the basin (47°20'N, 89°41'E) at an elevation of 1370 m a.s.l. Field measurements at the site include meteorological measurements, snow properties, frozen soil monitoring and so on. Meanwhile, meteorological measurements include air temperature ($\pm 0.4^\circ\text{C}$), relative humidity ($\pm 2\%$) (HMP45C probe, Vaisala, Helsinki, Finland) and wind speed ($\pm 0.3\text{ ms}^{-1}$) and direction (propvane 05103 anemometer, RM Young, Traverse City, Michigan) at a height of 3 m above the ground surface.

Snow property measurements include snow depth ($\pm 1\text{ cm}$) (Campbell SR50A snow depth sensor, Campbell Scientific, USA), SWE (snow pillow, 10389, Austria) and layered snow temperature ($\pm 0.5^\circ\text{C}$) (Campbell SI-111 infrared radiometer, Campbell Scientific, USA). Solid precipitation was measured in millimetres of water equivalent ($\pm 0.1\%$) using a Geonor T-200B accumulative weighing bucket precipitation gauge without heating (Campbell Scientific, USA). All sensors were connected to a data logger (CR1000, Campbell Scientific, USA), and the automatic weather station (AWS) recorded the half-hourly mean of measurements taken every 10 s. Other parameters such as layered soil temperature and soil moisture were also monitored. Four new net radiometers ($\pm 1\%$) (CNR4, Campbell Scientific, USA) were installed at the station in September 2013 to monitor incident and reflected shortwave radiation, and incoming and outgoing longwave radiation.

Description of the snowmelt model

Traditional degree-day models only consider air temperature, yet snowmelt processes are affected by many other factors. Enhanced TIMs have therefore been developed and widely applied because of their limited demands for *in situ* data and their high temporal and spatial resolution simulations of melt rates (Hock, 1999; Pellicciotti *et al.*, 2005). The following model has been shown to perform well and computes melt as the sum of two components (Pellicciotti *et al.*, 2005):

$$M = \begin{cases} \text{TFT} + \text{SRF}(1 - \alpha)G & T > T_T \\ 0 & T \leq T_T \end{cases} \quad (1)$$

where T is the cumulative positive average daily temperature over a given time, α is albedo and G is

incoming shortwave radiation (W m^{-2}). Calibrations of α are based on time after the snowfall event and accumulated daily maximum positive temperature. Incoming shortwave radiation was modelled using a parametric model for clear-sky conditions based on Corripio (2003). TF and SRF are empirical coefficients, being the temperature factor and shortwave radiation factor, expressed in millimetre per hour per degree Celsius and square metre millimetre per Watt per hour, respectively. These two coefficients need to be optimized using meteorological data-calculated hourly energy balance melt rates for the entire melt period. T_T is a threshold temperature below which no melting occurs.

The enhanced TIM is a sound approach, but there are many introduced parameters. Air temperature and net radiation were the key parameters considered in the modified TIM based on remote sensing data. Fieldwork and observations in the Kayeriesi River basin in recent years have shown that radiation, terrain, elevation and aspect all affect the snowmelt rate. In general, elevation directly affects temperature and indirectly affects snowmelt; terrain and aspect mainly affect the amount of radiation received by the Earth's surface. Based on measured field data and AWS observations, this study use a modified temperature index method coupled with high-resolution NCEP-based meteorology dynamically downscaled and spatially disaggregated to 1 km and remote sensing data to model spring snowmelt processes. The model is built as follows:

$$M_i = \text{DDFT}_{ai} + \text{NRFR}_{ni} + N \quad (2)$$

where the subscript i denotes a day in the time series, M_i is snowmelt SWE, T_{ai} is positive air temperature, R_{ni} is average positive net radiation, DDF is the 'temperature factor', NR is the 'net radiation factor' and N is a fixed constant term. Instantaneous distributed net radiation was calculated from incident shortwave radiation, albedo and incident longwave radiation as follows:

$$R_n = S_{in}(1 - \alpha) + L_{in} - L_{out} \quad (3)$$

where S_{in} is incident shortwave radiation, α is shortwave albedo, L_{in} is incident longwave radiation and L_{out} is outgoing longwave radiation. L_{out} was parameterized using the Stefan–Boltzmann law [$L_{out} = \epsilon\sigma T_s^4$, and T_s is land surface temperature (LST)]. Spatial α and T_s were obtained from remote sensing data. Spatial S_{in} and L_{in} are dynamically downscaled and statistically bias corrected and spatially disaggregated NCEP output.

The daily net radiation was parameterized from instantaneous radiation values at noon. Sequin and Itier (1983) pointed out that the relative contribution of noon net radiation to integrated daily radiation is

reasonably constant. This relationship can be expressed as follows:

$$R_{n,d} = CR_{n,s} \quad (4)$$

where C is the net radiation refractive coefficient, which represents the relationship between the two net radiation values, $R_{n,d}$ is integrated daily radiation, and $R_{n,s}$ is instantaneous net radiation at noon. For this study basin, $C=2.3$. Then, integrated daily radiation can be estimated sequentially.

To obtain high-resolution spatial SWE estimates in the study basin, daily distributed SWE was calculated as follows:

$$S_SWE_{i+1} = S_SWE_i + PRE_{i+1} - Melt_SWE_{i+1} \quad (5)$$

where S_SWE_{i+1} is SWE on $i+1$ day after snowmelt, S_SWE_i is distributed SWE, PRE_{i+1} is precipitation and $Melt_SWE_{i+1}$ is snowmelt SWE.

Key model parameters were selected from remote sensing data. The initial snow depth of the snowmelt model was from an improved microwave dataset from AMSR-E data based on *a priori* snow characteristics in Xinjiang, China (Che *et al.*, 2008; Dai *et al.*, 2012). The *a priori* snow characteristics include the snow grain size, snow density and temperature of the layered snowpack. The root mean squared error (RMSE) and bias from this new algorithm were greatly reduced compared with those of existing SWE products from the National Snow and Ice Data Center, moderately reduced compared with those of the European Space Agency and slightly reduced compared with those of the Environmental and Ecological Science Data Center for West China. Precipitation is low in spring in the study region, so AWS rainfall data were selected for use in the model to simulate temporal variations in river basin SWE.

Production of meteorological forcing data

The WRF model was used to downscale NCEP reanalysis fields to obtain 5-km-resolution meteorological data and was initialized using NCEP Final Analysis data with a resolution of $1 \times 1^\circ$ (111×111 km) (Pan *et al.*, 2014). The WRF model includes two-way nested computational horizontal resolutions of 25 and 5 km, respectively. Meteorological variables produced for spring (March–May) 2012 included 2-m temperature, surface pressure, 2-m relative humidity, shortwave and longwave radiation, wind fields and precipitation. The domain covered 47° – 49° N and 88° – 91° E. The dataset is in Lambert projection, and the temporal resolution of the data is 1 h.

The MicroMet method is a statistical downscaling method and is specifically designed to produce high-resolution

meteorological forcing data, and used to downscale the dataset from 5 to 1 km, which is the spatial resolution required for the snowmelt model in this study. The principle of the MicroMet model is to use known relationships between meteorological variables and the surrounding landscape (primarily topography) to distribute the variables over any given landscape in computationally efficient and physically plausible ways (Liston and Elder, 2006). In the method, the influences of cloud cover, direct and diffuse solar radiation, and topographic slope and aspect on incoming solar radiation were considered during solar radiation calculation (Liston and Elder, 2006). The specific equations and theory were described in the reference (Liston and Elder, 2006).

Estimation of DDF and NRF

Several methods can be used to obtain DDF observations, such as using ablation stakes (Liu *et al.*, 1998), lysimeters (Gild *et al.*, 1999) and energy balance calculations (Braithwaite *et al.*, 1998). For this study, the ablation stake method was considered most appropriate to obtain data at 1-km spatial resolution to match the size of remote sensing pixels.

Before the field observation experiment, we considered influencing factors such as experimental conditions and feasibility, and selected a field site at the outlet of the Kayiertesi River basin (elevation, 1370 m a.s.l.). The experiment covered the period 10–24 March 2014. A total of 26 stakes were established dispersedly in a 1×1 km grid, and the heights were measured at noon each day in the same sequence during the observation period to obtain the total ablation depth. The average value from the 26 observation stakes was used as the ablation depth value for the pixel.

Automatic weather station records show that air temperature was less than 0°C during 10–13 March 2014, but daily snow ablation was about 1 cm. It can thus be inferred that net radiation was the major control on snowmelt in this period. The NRF was calibrated to be 0.12 – 0.18 mm $\text{W m}^{-2} \text{day}^{-1}$ from observation. The daily ablation depth increased with time, with a maximum of 35 mm during the observation period. The DDF is calibrated to vary from 2.2 to 6 mm $^\circ\text{C}^{-1} \text{day}^{-1}$ from measurements during the study period. In this study, we used a DDF of 5.8 mm $^\circ\text{C}^{-1} \text{day}^{-1}$, an NRF of 0.17 mm $\text{W m}^{-2} \text{day}^{-1}$, and a constant term N of 9 mm. A measured mean snow density of 180 kg m^{-3} was used to convert snow depth into SWE during the study period.

The parameters of spatial α , T_s and initial snow depth

Key parameters for the model were selected from remote sensing data. Albedo data used in this study are from the Terra/Aqua Moderate Resolution Imaging

Spectroradiometer (MODIS) synthesis albedo (MCD43B3) with 1-km spatial resolution and 8-day temporal resolution. The MODIS albedo algorithm is derived from multiday, cloud-free, atmospherically corrected surface reflectance observations collected by the first seven land bands in the visible and near-infrared spectrum (Schaaf *et al.*, 2002; Wang *et al.*, 2010). LST used in this study is the MOD11 daily product with 1-km spatial resolution, gridded in a sinusoidal map projection. However, the MOD11 LST product is calculated with cloud cover, so in this study an interpolation method following the theory of similarity was used to remove cloud pixels (Yu *et al.*, 2015). This method estimates missing LST pixels using known LST pixel sets with similar LST variation characteristics as the missing pixels. Elevation strongly affects snow quantity and the distribution pattern. Snow depths increase with elevation up to a certain level to a distinct peak and then decreases at the highest elevations as a result of the redistribution of snow by wind, sloughing and avalanching (Grünwald *et al.*, 2014). Although the spatial resolution of the microwave data from Dai *et al.* (2012) was relatively coarse (25 km), it is better than point data to set the initial state of the snowmelt model, especially in areas with few observations of snow depth.

We used the MOD10A1 daily snow cover products to validate the model results. These data were used to map snow cover variations in the Kayiertesi River basin from March to June 2012 for comparison with model results. MOD10A1 daily products are available from the National Snow and Ice Data Center (Boulder, CO, USA) and include snow extent, snow albedo, fractional snow cover and quality assessment data, all gridded at 500-m resolution in a sinusoidal map projection. Cloud pixels were determined using the daily snow cover series, and snow cover maps were produced by compositing 3–5 days of the MOD10A1 product to find the maximum snow cover extent during a 5-day period. The intent of the algorithm in our study was similar to that of MOD10A2, which maximizes the number of snow pixels while minimizing the number of cloud pixels.

Evaluation method

Two quantitative statistical analysis methods (standard regression and error analysis) were used to evaluate parameters and model results. Standard regression statistics measure the linear relationship between simulated and observed values, and error analysis provides a quantitative assessment of the model output. Each statistical method applied in the performance evaluation has limitations, and thus, the study uses multiple assessment and evaluation methods including correlation coefficients (r), the mean error (ME), RMSE and the

Nash–Sutcliffe efficiency coefficient (NSE). The RMSE is a weighted measure of the difference between observations and simulations. The NSE was originally proposed by Nash and Sutcliffe (1970) and is a useful metric to evaluate and compare the performance of hydrologic models. It is described by

$$NSE = 1 - \frac{\sum (Q_{\text{calc}} - Q_{\text{obs}})^2}{\sum (\bar{Q}_{\text{obs}} - Q_{\text{obs}})^2} \quad (6)$$

where Q_{obs} is the observed streamflow, Q_{calc} is the predicted streamflow and \bar{Q}_{obs} is the mean observed flow over the interval of interest.

RESULTS

Validation of meteorological forcing data

Hourly observation data are available from the AWS site in the study basin. Temperature and radiation data are required for the snowmelt model in this study, so these two factors were validated using data from Kuwei station. Figure 2 shows the daily and hourly air temperature validation for the downscaling simulation of the Kayiertesi River basin. Results show that the air temperature simulation agrees well with AWS observations and captures the diurnal variation. The correlation coefficient (r) between daily downscaling simulations and AWS temperature is 0.95 ($P < 0.001$), and the ME and RMSE are 0.43 °C and 2.66 °C, respectively. The correlation coefficient between hourly downscaling simulations and AWS observations is 0.91 ($P < 0.001$), and ME and RMSE are 0.43 °C and 3.81 °C, respectively. The results indicate that downscaling simulations of air temperature are reliable for use in the snowmelt model regardless of whether daily or hourly validations are considered.

Figure 3a compares the observed and modelled hourly S_{in} . The watershed is located in the mountains with undulating terrain that causes an uneven distribution in solar energy reaching the surface in our study area. At a given height and time, solar radiation received at the surface varies widely with slope and aspect. Thus, the distribution of SWE is highly changed with solar radiation during snowmelt process. Scatterplots show that hourly simulations of S_{in} were also reasonable, with an R value for hourly downscaled simulations and AWS observations of 0.84 ($P < 0.001$) and ME and RMSE values of 28.2 and 163.5 W m^{-2} , respectively. Analysis of daily S_{in} shows that simulation results were consistent with observations and captured the diurnal variation in shortwave radiation. The downward shortwave radiation RMSE is acceptable for hydrological and snowmelt

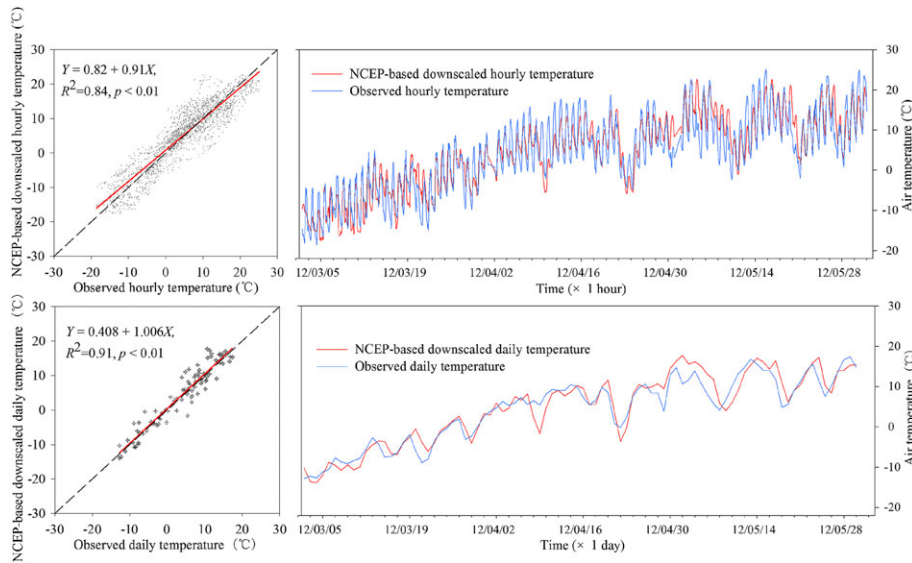


Figure 2. Comparison of National Centers for Environmental Prediction (NCEP)-based downscaled and observed air temperature at hourly and daily scales at Kuwei station in spring 2012. The regression line between downscaled and observation temperatures was incorporated in the scatterplot. The equations of the regression lines were also provided

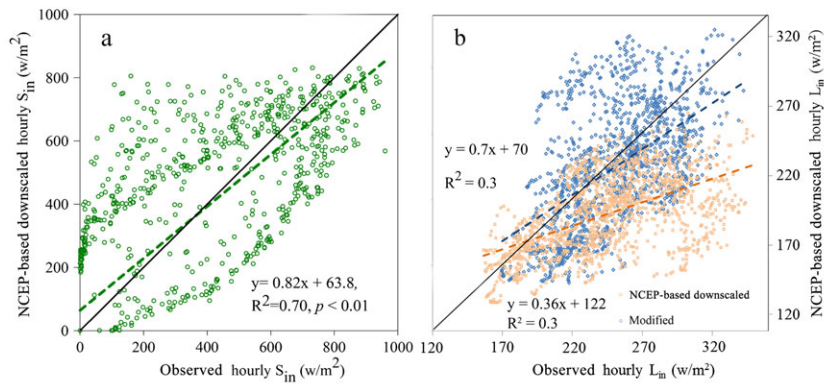


Figure 3. Comparison (a) between National Centers for Environmental Prediction (NCEP)-based downscaled and observed hourly shortwave radiations at Kuwei station in spring 2012 and (b) NCEP-based downscaled, modified NCEP-based downscaled and observed hourly longwave radiation at Kuwei station. The regression lines and linear equations between observation data and downscaled meteorological data were also shown in the figure

models in mountain areas, given the 10% instrument error.

Hourly L_{in} simulations are less accurate than those for shortwave radiation, and there is a small underestimation of L_{in} in the model results. We found that most of L_{in} was undervalued by around 20%. We therefore used an empirical statistic parameter of 1.2 to correct the bias of NCEP-based downscaled L_{in} value. This yielded a better agreement between observed L_{in} and modified L_{in} , with most of points scattered around the 1:1 line (Figure 3b), and an increase in the linear regression slope from 0.36 to 0.7. The modified L_{in} better captured observed values at an hourly scale.

The snowmelt model uses instantaneous S_{in} and L_{in} calculations to obtain daily R_n for estimating spatially distributed daily snowmelt. This modification will

improve the underestimate of instantaneous L_{in} and daily R_n , thereby reducing errors in snowmelt estimates in the remote sensing (RS)-based snowmelt model, particularly for mountainous regions.

Validation of α and T_s

The parameters α and T_s are important in the RS-based snowmelt model. Before using spatial α and T_s derived from remote sensing data, we validated these data to test their applicability in this study area. Figure 4 compares observed and MODIS albedo and LST. MODIS albedo was validated using measured data from 2014 because of installation of radiometers at this time; MODIS LST was validated using observed data from spring 2012. The results indicate strong correlations between observed and

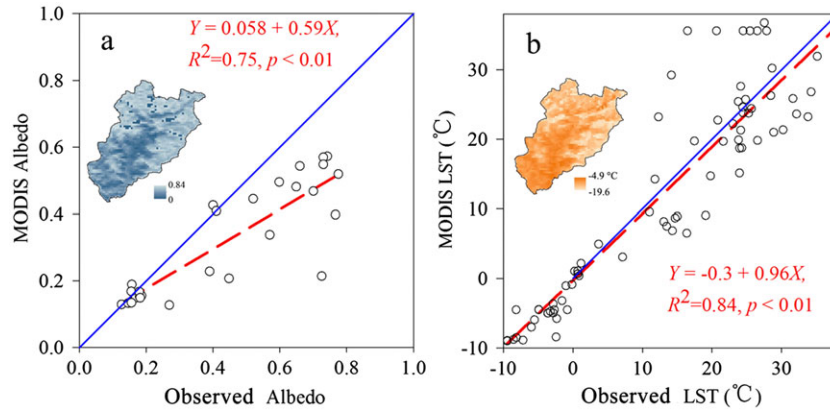


Figure 4. Scatterplots of (a) Moderate Resolution Imaging Spectroradiometer (MODIS) albedo and observed albedo and (b) MODIS and land surface temperature (LST) in spring 2012. The spatial distribution of MODIS albedo and MODIS LST in one day in the Kayiertesi River basin was inserted in (a) and (b), respectively

MODIS albedo and LST, with a regression coefficient of $R^2=0.75$ ($P<0.01$) for albedo and $R^2=0.84$ ($P<0.01$) for LST. Thus, both types of MODIS data are considered reliable for use in the RS-based snowmelt model.

SWE simulation in spring 2012

Based on the model calibration for the Kayiertesi River basin as described earlier, we simulated snowmelt processes from 1 March 2012 to the beginning of June 2012 to obtain high-resolution SWE variations in the basin. Figure 5 shows the spatial and temporal variations in SWE for the eight snowmelt days investigated. There are 2194 pixels in the basin with a spatial resolution of 1×1 km. The daily mean SWE of the basin was calculated by calculating SWE value from each pixel, so as to calculate the volume of SWE over the whole basin.

To verify the accuracy of the simulation results, we extracted the snow cover area from MOD10A1 remote sensing data (1 km resolution) on a daily basis. SWE variations compare well with snow cover obtained from MOD10A1 during the same period (Figure 5), which means that the variations in snow cover area and simulated SWE are consistent. The two snow cover ratio datasets from MOD10A1 and SWE simulated in this study are also showed in Figure 5. The snow cover area calculated from modelled SWE is a little higher than that from MOD10A1, but the maximum correlation coefficient is 0.98. The spatial variation in land surface parameters measured by remote sensing data is considered reasonable, and we therefore conclude that SWE simulations are close to reality. According to the model results, we calculated mean SWE and the SWE volume of the whole basin in different date. From 1 March to 25 May, mean SWE varied from 70.18 to 1.09 mm; snowmelt water volume varied from 154×10^6 to

2.4×10^6 m³. The snowmelt period lasted for approximately 3 months in spring 2012 in the basin.

Another validation method uses *in situ* snow depth to verify modelled results. Snow depth is recorded by a snow depth meter (Campbell SR50, ± 1 cm) at the outlet of the study basin. Simulated SWE was compared with observed data at this location (Figure 6a). The modelled SWE curve is close to the one from observation, and the decrease in modelled SWE is a close reflection of snowmelt processes at the outlet of the basin during March 2012. Furthermore, relative error analysis gives a maximum of 52.4%, a minimum relative error of 0.26%, and an average relative error of 6.7%. NSE is 0.98, which further verifies that the improved model simulations using spatial forcing data correspond well with observed values.

After 1 March, the solar height angle continues to increase, and the surface radiation balance also increases along with temperature. In this basin, snow gradually melted from low to high altitudes (Figure 6b). From early to late March 2012, melt rates of snow at the altitude of 1400, 1600 and 1800 m were close. They all melt away at the end of March. The melt rates at low altitudes were larger than those at high-altitude areas during this period. The snowmelt beginning time was delayed with altitude from 2000 to 3000 m (Figure 6b).

DISCUSSION

Daily snowmelt water volume was calculated in the Kayiertesi River basin for spring 2012 using modelled spatial SWE. As shown in Figure 7, daily snowmelt water volume increased with temperature in March, and peak snowmelt occurred at the end of March. The peak daily snowmelt volume was 5.3×10^6 m³ over the whole basin. However, there was high variation in daily snowmelt water volume in April with no obvious peak melt period.

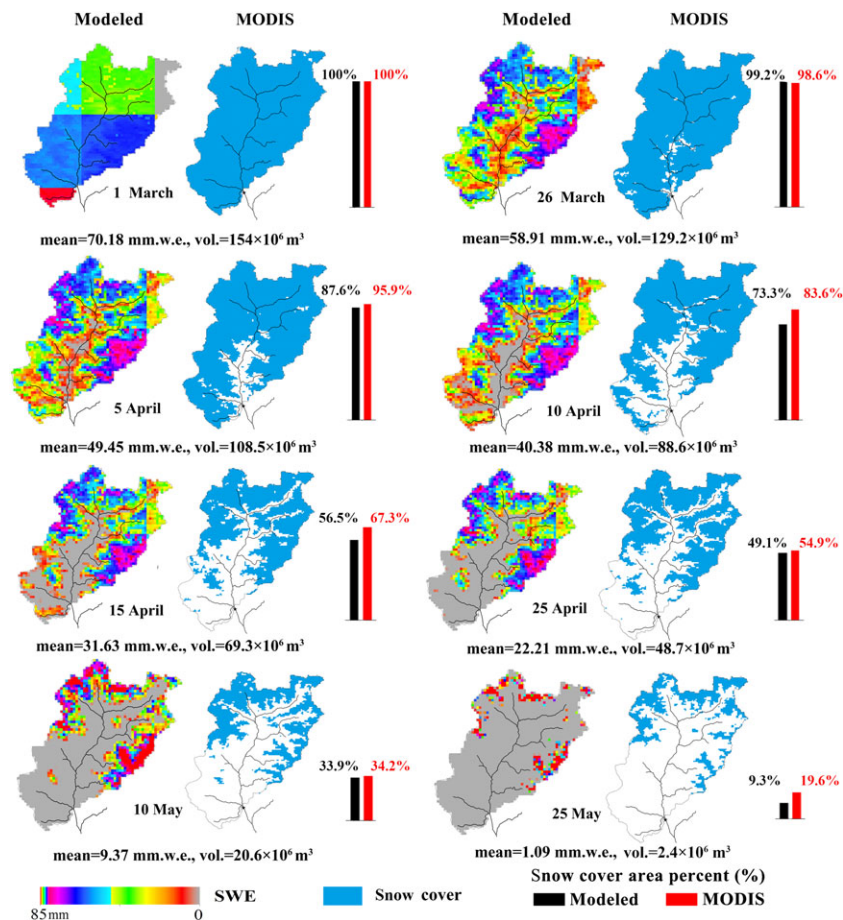


Figure 5. Spatiotemporal variations of modelled snow water equivalent (SWE) compared with the spatial distribution of snow cover from Moderate Resolution Imaging Spectroradiometer (MODIS) in spring 2012. The bars indicate snow cover area percentage (%) from model result and MODIS observation

There were four days in April when the amount of snowmelt run-off was near zero. At other times, the small amount of snowmelt run-off was affected by precipitation events. For example, precipitation recorded at the station was 1.6 mm on 1 April, 2.8 mm on 17 April, 5 mm on 28 April and 9.9 mm on 30 April. Precipitation can be divided into snow or rain, depending on whether the temperature is above or below a certain threshold (Vehviläinen, 1992; L'hôte *et al.*, 2005), which is most widely used for identification of precipitation types. In this study, we choose the widely used single-threshold method and 0°C as the threshold to discriminate the precipitation types. 0°C is a widely used temperature threshold and also has been validated in Xinjiang (Yang *et al.*, 1997; Clark *et al.*, 2006; Qing *et al.*, 2011; Duan *et al.*, 2012). Rainfall is often accompanied by windy and humid conditions, which can greatly accelerate snowmelt to produce more melt water in mountainous regions (Sui *et al.*, 2010). However, snowfall results in increased snow cover and slows down the rate of snowmelt and melt water release. Several phenomena may also occur

simultaneously at different elevations. For example, a valley may be bare in spring on hill slopes, and at high elevations snow may melt or accumulate. The basic elevation trend is affected by spatial variations in snow deposition, exposure and transport mechanisms (e.g. wind). On the four precipitation days in the study region, air temperature at the outlet of the basin at an altitude of 1370 m was no more than 10.9°C , assuming the change in temperature with elevation can be calculated using a temperature lapse rate of $-0.65^\circ\text{C}/100 \text{ m}$ (Gardner *et al.*, 2009). Snow fell in the basin on 1 April above 1960 m, and on 30 April above 3040 m. On this latter date, snow cover had melted below 2600 m (Figure 8). Thus, it is inferred that most of the precipitation over the basin over the four-day period fell as snow. In this case, temperature, radiation and the release of snowmelt water would have decreased. In May, there were also several peaks in 16–18 May and 25 May, but these were not as high as in April, because about 60% of snow cover had melted out. However, measures need to be taken to protect against flooding resulting from a large pulse in

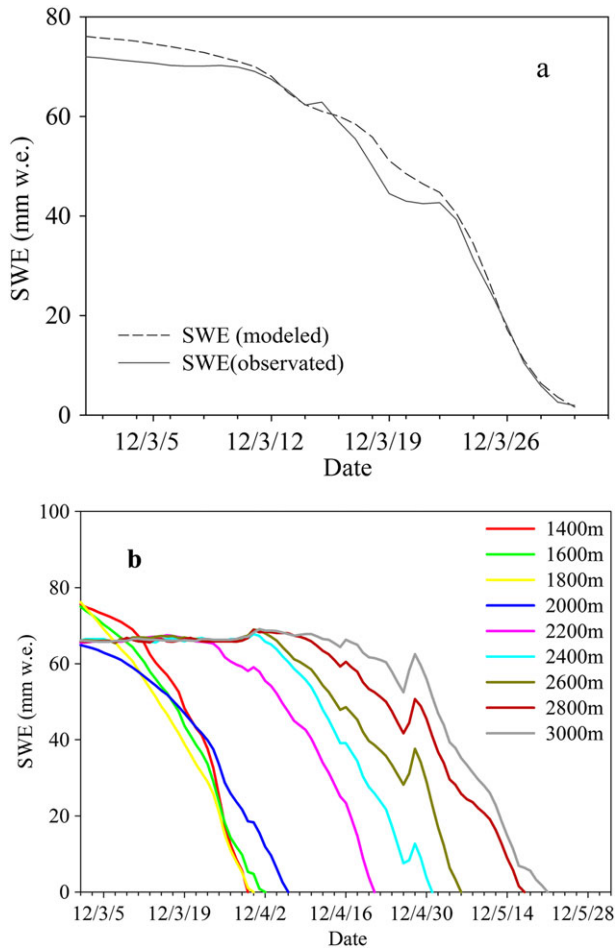


Figure 6. (a) Variation of modelled and observed snow water equivalents (SWEs) at the outlet of the basin over time. (b) Variation of modelled SWE at different elevations over time

snowmelt from unexpected heavy precipitation events during this period.

Snowmelt run-off in spring 2012 was calculated by assuming that snow cover was completely converted to run-off ($1.68 \times 10^8 \text{ m}^3$). Because of the lack of measured run-off data in the basin in 2012, this research used monthly run-off data from Kuwei Hydrological Station during 1959–2010 to make preliminary estimates of the

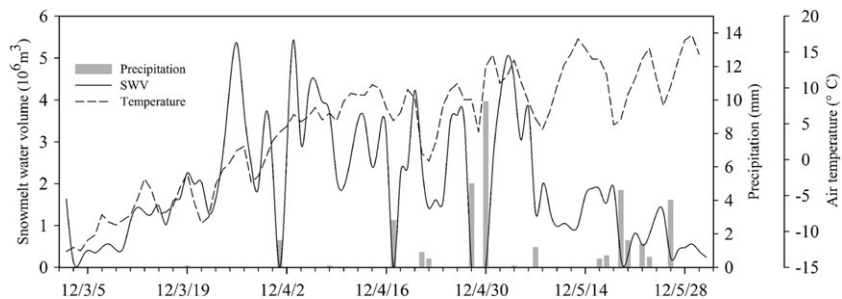


Figure 7. Variations of daily precipitation, daily snowmelt water volume (SWV) and daily mean temperature in the study basin during spring 2012

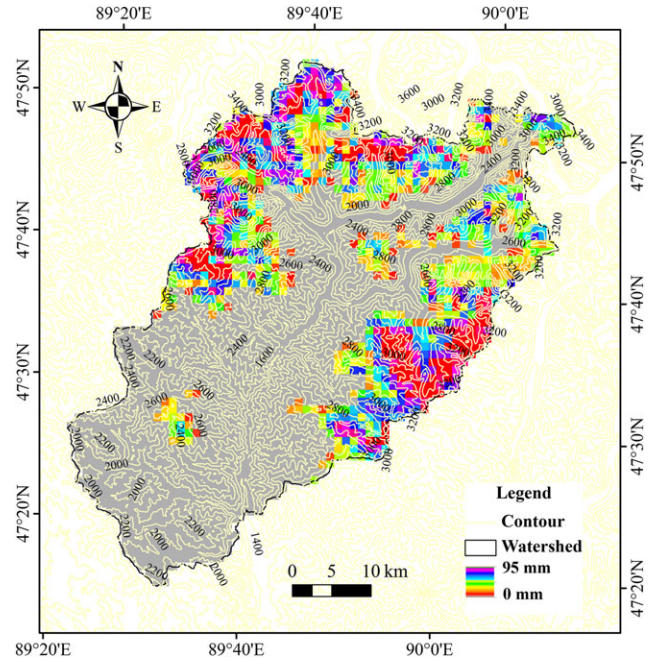


Figure 8. Distribution of modelled snow water equivalent in the study basin on 30 April 2012

proportion of snowmelt run-off in the basin. The average annual run-off in the study basin in 1959–2010 was $8 \times 10^8 \text{ m}^3$, and average spring (March to May) run-off was $2.33 \times 10^8 \text{ m}^3$.

According to snowmelt simulations in this study, spring snowmelt run-off accounted for 72.1% of spring run-off in 2012 and 21% of annual run-off. This shows that a high proportion of snowmelt run-off is a significant characteristic of mountainous watersheds in the Altay Mountains. In comparison, for the Kelan River, a branch of the Ertix River on the southern slopes of the Altay Mountains, 45% of annual basin flow is derived from snowmelt (Shen *et al.*, 2007). However, for the upper Yellow River, annual snowmelt run-off accounts for 20% of annual run-off from the basin (Wang and Shi, 2000). The proportion of snowmelt run-off relative to the total run-off from late March to late June was 55.9% in Shule River, which is located in the western Qilian Mountains

and is also affected by westerly winds. In Shule River basin, the proportion of snowmelt run-off relative to the annual run-off was only 15.4%. Compared with these results, the proportion of snowmelt run-off in our study basin is high. This further illustrates that snowmelt water is typically the most important source of spring run-off in basins in the Altay Mountains.

Snowmelt run-off is strongly affected by weather and climate change and varies year by year as well as in long-term scales. As snowmelt plays an important role in regulating the downstream river flow in the studied basin, further research into relationships between snowmelt and mountain water resources not only has great scientific significance, but is also important to the region's economic development. For example, in heavy snowy year, if snowmelt in the upstream of the basin came earlier than that in normal year, it may cause snowmelt flood which threaten cropland, agricultural activities and life in the downstream. However, in less snow year, because snowmelt in the upstream plays an important role as water resource in spring, it would be not sufficient to irrigate cropland in the downstream and influence agriculture economic development. The results of this study also provide a basis for snowmelt flood prevention. The results of this study can provide a good method to calculate volume of run-off generation, and it can prepare for run-off concentration. Thus, the time of peak flood could be calculated precisely in the basin, which has the benefits of snowmelt flood prevention in the downstream of the basin and reduction of damage from snowmelt floods.

CONCLUSIONS

This study simulated snowmelt in the Kayiertesi River catchment in spring 2012 using a TIM that was improved using a combination of remote sensing data, *in situ* observations and a short-term observational campaign, driven by NCEP-based meteorology, downscaled using WRF and a statistical bias correction/spatial disaggregation model. Our results indicate that use of downscaled, bias-corrected and spatially disaggregated NCEP meteorology to drive the snowmelt model significantly improves the quality of spatial meteorological data. Using remote sensing data in the improved snowmelt model reduces the number of parameterizations, and also makes it easy to apply the model in data-scarce regions.

The use of forcing data to produce reliable SWE simulations in spring 2012 in this study also provides insight into temporal SWE variations in mountainous basins. Daily variations in snowmelt water volume and the proportion of snowmelt run-off were also analysed and calculated. Snowmelt water is the main run-off source

in the catchment and should be managed and fully utilized. The results also provide a basis for the prevention of snowmelt-induced flooding.

Future work should further explore climatological controls on TIM parameters to determine the transferability of our approach to other regions and to spatially distributed simulation approaches across large and/or data-sparse catchments. In this basin, an applicable concentration model needs to be built, and then peak discharge in a year could be forecasted; one or two other watersheds in Xinjiang will be chosen to apply the method of this study.

ACKNOWLEDGEMENTS

The authors thank NASA for providing image data, and the Kuwei Snow and Hydrological Observation Station for providing meteorological data. This work was supported by the National Natural Science Foundation of China (grant nos. 41190084, 41271083 and 41471292), the Open Foundations of the State Key Laboratory of Frozen Soil Engineering, Chinese Academy of Sciences (grant no. SKLFSE201412) and CAS Bureau of International Cooperation Foundation 'Central Asia ice and snow resources change and its impact on water resources' (Y560L01001). We also acknowledge field staff from the Kuwei National Basic Hydrological Station, Bin He and Feng Diao, for their assistance in collecting field data. We also thank anonymous reviewers and the journal editor, whose comments and suggestions helped to improve the quality of this paper.

REFERENCES

- Box JE. 2013. Greenland ice sheet mass balance reconstruction. Part II: Surface mass balance (1840–2010). *Journal of Climate* **26**: 6974–6989.
- Braithwaite RJ, Konzelmann T, Marty C, Olesen OB. 1998. Errors in daily ablation measurements in northern Greenland, 1993–94, and their implications for glacier climate studies. *Journal of Glaciology* **44**: 583–588.
- Che T, Xin L, Jin R, Armstrong R, Zhang T. 2008. Snow depth derived from passive microwave remote-sensing data in China. *Annals of Glaciology* **49**: 145–154.
- Clark MP, Slater AG, Barrett AP, Hay LE, McCabe GJ, Rajagopalan B, Leavesley GH. 2006. Assimilation of snow covered area information into hydrologic and land-surface models. *Advance Water Resource* **29**: 1209–1221.
- Corripio JG. 2003. Vectorial algebra algorithms for calculating terrain parameters from DEMs and solar radiation modelling in mountainous terrain. *International Journal of Geographical Information Science* **17**: 1–23.
- Dai L, Che T, Wang J, Zhang P. 2012. Snow depth and snow water equivalent estimation from AMSR-E data based on *a priori* snow characteristics in Xinjiang, China. *Remote Sensing of Environment* **127**: 14–29.
- Dozier J, Painter TH. 2004. Multispectral and hyperspectral remote sensing of alpine snow properties. *Annual Review of Earth and Planetary Sciences* **32**: 465–494.

- Duan K, Yao T, Wang N, Liu H. 2012. Numerical simulation of Urunch Glacier No. 1 in the eastern Tianshan, central Asia from 2005 to 2070. *Chinese Science Bulletin* **57**: 3511–3515.
- Gao H, He X, Ye B, Pu J. 2012. Modeling the runoff and glacier mass balance in a small watershed on the Central Tibetan Plateau, China, from 1955 to 2008. *Hydrological Processes* **26**: 1593–1603.
- Gardner AS, Sharp MJ, Koerner RM, Labine C, Boon S, Marshall SJ, Burgess DO, Lewis D. 2009. Near-surface temperature lapse rates over Arctic glaciers and their implications for temperature downscaling. *Journal of Climate* **22**: 4281–4298.
- Gild CE, Knudby CJ, Knudsen MB, Starzer W. 1999. Snowmelt and runoff modelling of an Arctic hydrological basin in west Greenland. *Hydrological Processes* **13**: 397.
- Grünwald T, Bühler Y, Lehning M. 2014. Elevation dependency of mountain snow depth. *The Cryosphere* **8**: 2381–2394.
- Hock R. 1999. A distributed temperature-index ice-and snowmelt model including potential direct solar radiation. *Journal of Glaciology* **45**: 101–111.
- Hock R. 2003. Temperature index melt modelling in mountain areas. *Journal of Hydrology* **282**: 104–115.
- IPCC. 2013. Climate Change 2013: The Physical Science Basis. Contribution of Working Group I to the Fifth Assessment Report of the Intergovernmental Panel on Climate Change. Cambridge University Press, Cambridge, United Kingdom and New York, USA, 40–46 pp.
- Irvine-Fynn TDL, Hanna E, Barrand NE, Porter PR, Kohler J, Hodson AJ. 2014. Examination of a physically based, high-resolution, distributed Arctic temperature-index melt model, on Midtre Lovénbreen, Svalbard. *Hydrological Processes* **28**: 134–149.
- Jost G, Moore RD, Smith R, Gluns DR. 2012. Distributed temperature-index snowmelt modelling for forested catchments. *Journal of Hydrology* **420**: 87–101.
- L'hôte Y, Chevallier P, Coudrain A, Lejeune Y, Etchevers P. 2005. Relationship between precipitation phase and air temperature: comparison between the Bolivian Andes and the Swiss Alps/Relation entre phase de précipitation et température de l'air: comparaison entre les Andes Boliviennes et les Alpes Suisses. *Hydrological Sciences Journal* **50**: 989–997.
- Liu S, Ding Y, Wang N, Xie Z. 1998. Mass balance sensitivity to climate change of the Glacier No. 1 at the Urumqi River Head, Tianshan Mts. *Journal of Glaciology and Geocryology* **20**: 10–14 (In Chinese).
- Liston GE, Elder K. 2006. A meteorological distribution system for high-resolution terrestrial modeling (MicroMet). *Journal of Hydrometeorology* **7**: 217–234.
- Ma H, Liu Z, Liu Y. 1991. Energy balance of a snow cover and simulation of snowmelt in the western Tien Shan Mountains, China. *Annals of Glaciology* **16**: 73–78.
- Matthews T, Hodgkins R, Wilby RL, Guðmundsson S, Pálsson F, Björnsson H, Carr S. 2015. Conditioning temperature-index model parameters on synoptic weather types for glacier melt simulations. *Hydrological Processes* **29**: 1027–1045.
- Nash J, Sutcliffe JV. 1970. River flow forecasting through conceptual models part I – a discussion of principles. *Journal of Hydrology* **10**: 282–290.
- Ohmura A. 2001. Physical basis for the temperature-based melt-index method. *Journal of Applied Meteorology* **40**: 753–761.
- Pan X, Li X, Shi X, Han X, Luo L, Wang L. 2012. Dynamic downscaling of near-surface air temperature at the basin scale using WRF – a case study in the Heihe River Basin, China. *Frontiers of Earth Science* **6**: 314–323.
- Pan X, Li X, Yang K, He J, Zhang Y, Han X. 2014. Comparison of downscaled precipitation data over a mountainous watershed: a case study in the Heihe River Basin. *Journal of Hydrometeorology* **15**: 1560–1574.
- Pellicciotti F, Brock B, Strasser U, Burlando P, Funk M, Corripio J. 2005. An enhanced temperature-index glacier melt model including the shortwave radiation balance: development and testing for Haut Glacier d'Arolla, Switzerland. *Journal of Glaciology* **51**: 573–587.
- Qing W, Chen R, Liu S, Han H, Wang J. 2011. Research and application of two kinds of temperature-index model on the Koxkar Glacier. *Advances of Earth Science* **26**: 409–416 (In Chinese with English abstract).
- Reeh N. 1989. Parameterization of melt rate and surface temperature on the Greenland ice sheet. *Polarforschung* **59**: 113–128.
- Rice R, Bales RC. 2010. Embedded-sensor network design for snow cover measurements around snow pillow and snow course sites in the Sierra Nevada of California. *Water Resources Research* **46**W03537: 1–13.
- Schaaf CB, Gao F, Strahler AH, Lucht W, Li X, Tsang T, Strugnell NC, Zhang X, Jin Y, Muller J-P. 2002. First operational BRDF, albedo nadir reflectance products from MODIS. *Remote Sensing of Environment* **83**: 135–148.
- Sequin B, Itier B. 1983. Using midday surface temperature to estimate daily evaporation from satellite thermal IR data. *International Journal of Remote Sensing* **4**: 371–383.
- Shen Y, Su H, Wang G, Mao W, Wang S, Han P, Wang N, Li Z. 2013. The responses of glaciers and snow cover to climate change in Xinjiang (II): hazards effects. *Journal of Glaciology and Geocryology* **35**: 1355–1370 (In Chinese).
- Shen Y, Wang G, Su H, Han P, Gao Q, Wang S. 2007. Hydrological processes responding to climate warming in the Upper Reaches of Kelan River Basin with snow-dominated of the Altay Mountains region, Xinjiang, China. *Journal of Glaciology and Geocryology* **29**: 845–854 (In Chinese).
- Sui J, Koehler G, Krol F. 2010. Characteristics of rainfall, snowmelt and runoff in the headwater region of the Main River Watershed in Germany. *Water Resources Management* **24**: 2167–2186.
- Vehviläinen B. 1992. *Snow Cover Models in Operational Watershed Forecasting*. National Board of Waters and the Environment: Helsinki, Finland.
- Wang K, Liang S, Schaaf CL, Strahler AH. 2010. Evaluation of moderate resolution imaging spectroradiometer land surface visible and short-wave albedo products at FluxNet sites. *Journal of Geophysical Research: Atmospheres (1984–2012)* **115**D17107: 1–8.
- Wang G, Shi Z. 2000. Impacts of climate change on hydrology in Upper Reaches of the Yellow River. *Henan Meteorology* **4**: 20–22 (In Chinese).
- Yu W, Nan Z, Wang Z, Chen H, Wu T, Zhao L. 2015. An effective interpolation method for MODIS land surface temperature on the Qinghai-Tibet Plateau. *IEEE Journal of Selected Topics in Applied Earth Observations and Remote Sensing* **8**: 4539–4550.
- Yang ZL, Dickinson RE, Robock A, Vinnikov KY. 1997. Validation of the snow submodel of the biosphere-atmosphere transfer scheme with Russian snow cover and meteorological observational data. *Journal of Climate* **10**: 353–373.
- Zhao Q, Liu Z, Ye B, Qin Y, Wei Z, Fang S. 2009. A snowmelt runoff forecasting model coupling WRF and DHSVM. *Hydrology and Earth System Sciences* **13**: 1897–1906.